Dual-Scale Pattern Formation in Nanoparticle Assemblies

Andrew Stannard,* Christopher P. Martin, Emmanuelle Pauliac-Vaujour, and Philip Moriarty

School of Physics and Astronomy, University of Nottingham, University Park, Nottingham NG7 2RD, UK

Uwe Thiele

School of Mathematics, Loughborough University, Loughborough, Leicestershire, LE11 3TU, UK, and Max-Planck-Institut für Physik komplexer Systeme, Nöthnitzer Str. 38, D-01187 Dresden, Germany

Received: April 18, 2008; Revised Manuscript Received: July 30, 2008

A pseudo-3D lattice gas-based Monte Carlo simulation is used to reproduce dual-scale nonequilibrium structures formed from drying colloidal nanoparticle solutions. Morphologies possessing multiple length scale features are recreated by coupling the chemical potential to the solvent density, modeling a film thickness-dependent disjoining pressure. By assigning a sigmoidal form to the chemical potential, a switch in the dewetting mechanism at a threshold solvent density is capable of producing nanoparticle patterning at two length scales. Dual-scale cellular networks, and nanoparticle ring and fingering structures coexisting with small scale patterning, can all be generated in this way with suitable simulation parameters. Extensive exploration of the model's parameter space maps the temperature-dependent spinodal line and demonstrates the influence of nanoparticle concentration on morphology.

I. Introduction

When colloidal nanoparticles are deposited from solution onto a substrate, a wide variety of spontaneous nonequilibrium patterns can form. These include self-organized structures such as isolated islands and wormlike domains, continuous labyrinthine and network structures, viscous fingering-like fractal structures, and micrometer-sized rings.[1−8] Both nucleation and growth and spinodal mechanisms are responsible for many of these structures; the morphology of deposited nanoparticles gives evidence of the solvent flow history prior to complete evaporation. In recent years, a variety of deposition techniques have been implemented to direct nanoparticle organization to create long-range ordered superlattices[9,10] and spatially controlled patterns.[11−13] Novel approaches to manipulate the spatial properties of nanoparticle assemblies have been implemented: both predeposition, via patterning substrates lithographically[14] and nonlithographically,[15] and postdeposition, via mechanically[16] and thermally activated coarsening.[17]

In 2003, Rabani et al.[17] introduced a model capable of reproducing many of these self- and template-organized patterns[14] via a two-dimensional lattice gas-based Monte Carlo simulation. In this model the interplay between solvent evaporation and nanoparticle diffusion leads to the formation of various nonequilibrium structures. Morphologies produced via the Rabani et al. model are homogeneous in the sense that a single type of patterning is observed across the entire simulation grid. Experimentally, however, nanoparticle assemblies formed via deposition from solution frequently comprise patterns on multiple length scales resulting from various solvent dewetting mechanisms. These morphologies are not observed in the original Rabani et al. model as the dewetting mechanism does not alter during the simulation and is governed by the initial parameters. A fully three-dimensional equivalent Monte Carlo simulation has been developed[18−20] and shown to demonstrate behavior unseen in the original 2D model. However, recent experiments[8] have confirmed that in many cases self-organization of nanoparticles far from equilibrium occurs within a 2D subsystem, making a fully 3D model redundant to some extent for the behavior of nanoparticles in the system of interest here. Indeed, our experiments, similar to previous studies,[18] generally focus on 2D systems where nanoparticle assemblies resulting from homogeneous solvent evaporation only have features which are one nanoparticle high. Structures with two or more layers of nanoparticles only occur when the nanoparticle concentration in the solution is increased or when topographic features induce defect nucleation of the solvent film at very early times during the dewetting process.

Here we show that by coupling the chemical potential to solvent density in the model of Rabani et al.,[17] we are able to form self-organized patterns possessing multiple length scale structures that emerge from different dewetting mechanisms. Although our simulation model is strictly 2D, this modification mimics to some extent the 3D nature of the solvent film thinning. As such, we describe here a pseudo-3D Monte Carlo simulation model, i.e., a 2D model which includes a dependence of the chemical potential on the solvent coverage to model a thickness-dependent disjoining pressure. Through extensive study of the original 2D model's parameter space we explore the temperature dependence of the spinodal line and show how passing through this line during a simulation allows the coexistence of nucleation and growth and spinodal dewetting patterning in our pseudo-3D model, as observed experimentally. We also explore the effect of nanoparticle concentration on the resulting morphologies to assess how varying the concentration modifies results obtained from a classic lattice gas model, highlighting that characterizing dewetting mechanisms solely from a final morphology can be problematic. Finally, we explore the parameter space resulting from the assignment of a sigmoidal form to the chemical potential. This modification is capable of creating experimentally observed morphologies with two distinct coexisting types of patterning such as dual-scale cellular networks

* Corresponding author. E-mail: ppxas1@nottingham.ac.uk.

10.1021/jp803399d CCC: $40.75
Published on Web 09/09/2008

and the coexistence of nanoparticle rings or viscous fingering-like fractal structures surrounded by small scale patterning.

In section II we introduce the model and discuss the solvent dewetting mechanisms that are observable in Monte Carlo simulations. In particular, we focus on the temperature and chemical potential dependence. In section III we first present results from exploration of the parameter space of the Rabani et al. model. We then proceed to describe how dual-scale nanoparticle morphologies may arise from a modification to this model. Experimental images are presented in conjunction with simulated morphologies which display a high degree of similarity. Finally, in section IV, we summarize our work and comment on future improvements to this model.

II. Simulation Model

In this section we describe our pseudo-3D lattice gas-based Monte Carlo simulation model, introducing a functional form of the chemical potential. We also discuss the dependence of the model's parameters on the solvent dewetting mechanism.

A. Monte Carlo Model. Although slightly complicated by the inclusion of nanoparticles, the simulation model is essentially a simple 2D lattice gas. Each cell of a square lattice, i, is occupied by either solvent, in liquid ($l_i = 1$, $v_i = 0$) or vapor ($l_i = 0$, $v_i = 1$) phase, or by a nanoparticle ($n_i = 1$); the presence of a nanoparticle excludes the presence of solvent. Solvent occupies single cells of the lattice whereas nanoparticles occupy 3 by 3 cells. The initial configuration of the simulation is a predefined concentration of nanoparticles randomly positioned on the lattice with all other lattice sites occupied by liquid, mimicking a thin film of a solvent−nanoparticle solution. The competing processes of solvent evaporation and nanoparticle diffusion are considered in turn. First, each solvent cell is examined in a four-phase checkerboard pattern, and an attempt is made to convert the solvent phase from liquid to vapor (or vice versa) with a Metropolis acceptance probability, p_{acc}, given by

$$p_{acc} = \min[1, \exp(-\Delta E/k_B T)] \quad (1)$$

where ΔE is the change in energy associated with such a move, and $k_B T$ is the thermal energy of the system. After each solvent cell has been examined, each nanoparticle is examined, and an attempt to move it by one lattice spacing in a random lattice direction is undertaken, again with probability p_{acc}. Nanoparticles may only move into wet areas of the lattice, that is, in a direction currently occupied by three adjacent liquid cells; this imitates low nanoparticle mobility on a substrate in the absence of solvent.[21] If the nanoparticle moves, the displaced liquid cells are positioned in the nanoparticle's wake to preserve solvent density. To gain control over the rate of nanoparticle diffusion relative to solvent evaporation, each nanoparticle is examined a number of times, given by the mobility ratio (MR), per solvent cycle. Single Monte Carlo steps (MCS) are defined as one solvent cycle followed by MR nanoparticle cycles.

The Hamiltonian used in our simulations is

$$E = -\epsilon_l \sum_{\langle ij \rangle} l_i l_j - \epsilon_n \sum_{\langle ij \rangle} n_i n_j - \epsilon_{nl} \sum_{\langle ij \rangle} n_i l_j + \mu(\nu) \sum_i l_i \quad (2)$$

where ϵ_l, ϵ_n, and ϵ_{nl} are the energies of liquid−liquid, nanoparticle−nanoparticle, and nanoparticle−liquid interactions, respectively, and μ is the chemical potential as a function of $\nu = \sum_i v_i / \sum_i (l_i + v_i)$, the fraction of solvent in the vapor phase. (Note that for convenience the sign of μ in eq 2 is changed with respect to previous work; here, μ is technically the negative of the thermodynamic chemical potential.) To ensure that nanoparticles are well solvated by the liquid prior to solvent dewetting, the interaction energies are chosen as $\epsilon_{nl} = 1.5\epsilon_l$ and $\epsilon_n = 2\epsilon_l$; these values are used throughout. Thus, if we also express thermal energy $k_B T$ and chemical potential μ in units of ϵ_l, we have only two independent energy scales. Equation 2 is identical to that used by Rabani et al.,[17] with the exception of the modification of the final term. This coupling of chemical potential to solvent density is designed to replicate a thickness-dependent disjoining pressure[14,22] which accounts for substrate wettability in continuum models;[23,24] this will be discussed in more detail later. Initially, however, final morphologies from simulations involving constant chemical potential values will be explored.

As the simulation progresses, the liquid phase of the solvent is converted to its equilibrium density; the chemical potential plays the major role in determining this value. In a classic lattice gas model, $\mu = 2\epsilon_l$ defines the binodal line where both solvent phases are equally favorable, when $\mu > 2\epsilon_l$, vapor is energetically more favorable. We can expect that for low nanoparticle concentrations the binodal line argument holds to a good approximation,[25] and so we perform simulations with $\mu > 2\epsilon_l$. Thus, liquid is converted to vapor, and commencing the simulation corresponds to a quench from $\mu = -\infty$. When using a sufficiently high mobility ratio, the nanoparticles are able to diffuse away from retreating liquid fronts to remain solvated and essentially map the history of dewetting prior to complete solvent evaporation. It should be noted that our reference to "complete solvent evaporation" does not include the evaporation of the liquid that remains as a stable wetting layer around nanoparticles due to the ϵ_{nl} interaction term. Certain simulation parameters favor a wetting layer which promotes coarsening of nanoparticle assemblies after the initial evaporation stage. Therefore, there are two time scales associated with these simulations: an evaporation time and a coarsening time. In this work we are concerned only with simulation morphologies after the initial evaporation stage, i.e., before significant coarsening has occurred. As such, simulation morphologies that are used as a comparison with experimental images (Figures 3a, 5a, and 6a) represent "sticky" structures; i.e., they do not evolve in time at any significant rate as a wetting layer is not stable.

The interactions between lattice cells are limited to nearest and next-nearest neighbors, which are given a weighting of 1 and $1/\sqrt{2}$ respectively, reflecting a linear decay in interaction strength with distance.[26] A renormalization factor of $1/(1/\sqrt{2} + 1)$ is then used to multiply the interaction energies such that the global energy is the same as for the nearest-neighbor only model. The parameter space associated with ϵ_l, μ, and $k_B T$ can therefore be compared to that of the classic lattice gas.

B. Dewetting Mechanisms. The solvent dewetting mechanism is primarily determined by the parameters μ and $k_B T$ (the same as those in a classic lattice gas model), and so exploration of this parameter space is key to understanding this model. There is clearly a vast parameter space associated with the model which in our case is further complicated by the functional form of the chemical potential; approaches have been put forward to efficiently explore the space.[27] In this work, we simulate some of the more striking and varied patterns that are observed from drying colloidal nanoparticle solutions.

Nucleation and growth occurs when the probability of liquid-to-vapor conversion is low enough such that only a few random positions in the solvent film are able to nucleate and grow

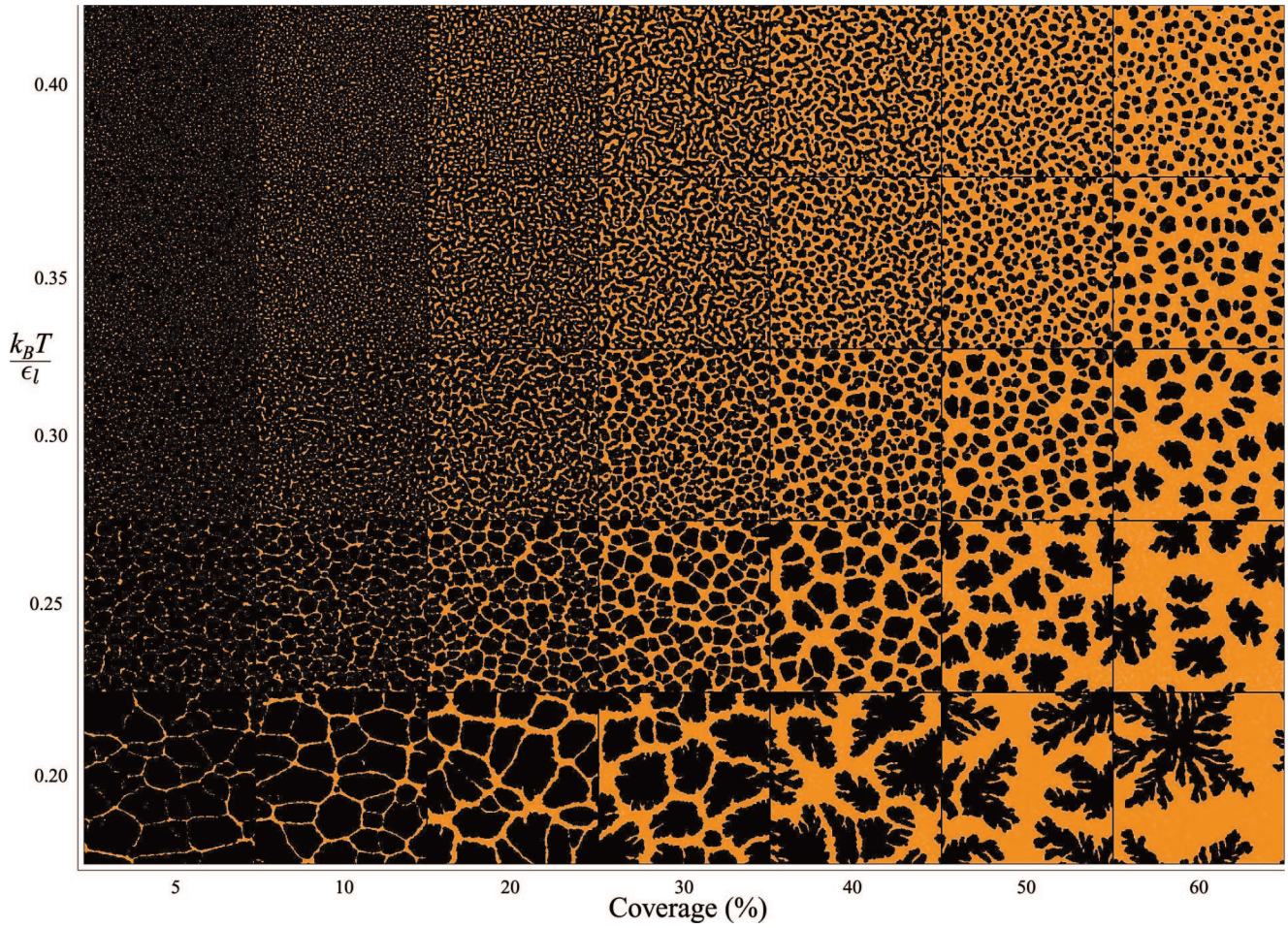

Figure 1. Morphology diagram of final nanoparticle positions resulting from varying nanoparticle concentration and temperature. All simulations were run on a 1024 × 1024 lattice with $\mu/\epsilon_l = 2.50$ and $MR = 30$. On the basis of an inspection of nanoparticle pattern morphology, a transition from nucleation and growth to spinodal dewetting occurs around $k_B T/\epsilon_l = 0.30$. The upper-right section shows that with high enough nanoparticle concentration spinodal dewetting can result in isolated holes, a structure not to be confused with the cellular networks (lower-left section) formed via nucleation and growth.

beyond some critical size at which further growth is energetically favorable. In this region of parameter space the initial liquid layer is in a metastable state; small local fluctuations in solvent density can be recovered, but large enough fluctuations nucleate holes in the film. The resulting final morphology is a cellular network which forms via the growth of holes in the thin film. These holes can either coalesce; create a thin, compact region of nanoparticles that form the network branches; or form network nodes at the junction of three of more holes. Despite the random positions of the initial nucleation sites, the final structure possesses spatial correlations (determined via morphological image analysis) due to the growth process through which it forms.[26]

As the temperature or chemical potential is increased, nucleation becomes more frequent, resulting in morphologies where the characteristic length scale decreases. The system is still metastable and dewetting is nucleation and growth dominated, but smaller local fluctuations are required to nucleate holes. Further increasing either of these parameters results in dewetting across the entire solvent−nanoparticle film within a very short time window—a signature of spinodal dewetting. This mechanism produces morphologies formed with a typical length scale—a spinodal wavelength. In this regime, the nanoparticle−solvent film rapidly progresses toward the solvent equilibrium density. These two mechanisms occur at different simulation parameters, and the temperature-dependent spinodal line, $\mu_{sp}(T)$, roughly corresponds to the separating line between the nucleation and growth-dominated and spinodal-dominated regimes.[17] For a discussion of related issues for a continuum model of dewetting for simple nonvolatile liquids see ref 28.

III. Results and Discussion

In this section we present the results of our simulations. First we explore the parameter space of the original Rabani et al.[17] model to eludicate the effect of certain parameters on the resulting deposited nanoparticle morphology. We then expand this model to reproduce dual-scale patterning by coupling the chemical potential to solvent density via a sigmoidal function.

A. Parameter Space Exploration. Clearly the introduction of nanoparticles into a lattice gas model will affect the dynamics of the problem, with an increasing nanoparticle concentration causing a greater shift from the classic lattice gas model. Figure 1 shows a morphology diagram associated with a section of the model's parameter space with varying nanoparticle concentration and temperature. When increasing the temperature at intermediate concentrations (20% or 30% are clearest), there is a transition from interconnected cellular network morphologies, characteristic of nucleation and growth, to labyrinthine structures and isolated wormlike domains and islands, characteristic of spinodal dewetting. However, increasing the nanoparticle concentration can make spinodal patterns appear as what seem

to be spatially correlated voids, which could be misinterpreted as a nucleation and growth pattern. In addition, significantly reducing the nanoparticle concentration can result in nucleation and growth-driven dewetting, giving rise to isolated wormlike and island structures, as the nanoparticles are driven to the network nodes, therefore leaving branches ill-defined. Hence, when choosing a nanoparticle concentration to give an accurate representation of the dewetting process purely from a final morphology, these factors must be considered and an optimal concentration must be used. Here we decide that a 25% nanoparticle concentration gives a fair transition from nucleation and growth to spinodal dominated dewetting from rudimentary analysis of final morphology.

For the simulations shown in Figure 1, we set the nanoparticle mobility ratio to be $MR = 30$. With this value, nanoparticles can diffuse away from liquid−vapor interfaces and remain mobile in solution when using chemical potential values close to the binodal value. As temperature is increased, time scales for both nanoparticle diffusion and solvent evaporation decrease, but the ratio maintains approximately constant. However, because the chemical potential directly affects the solvent evaporation, an increased chemical potential reduces the solvent evaporation time but has a weaker, indirect effect on the nanoparticle diffusion time scale. Thus, at high chemical potentials, nanoparticles cannot diffuse away from retreating liquid fronts fast enough, instabilities form at the solvent interface, and nanoparticles are deposited perpendicular to the front in the form of nanoparticle fingering structures. For the purposes of this work, the mobility ratio *MR* is considered to be the defining influence on nanoparticle fingering, as most simulations are run with chemical potential values near the binodal line and with intermediate nanoparticle concentrations. Figure 1 shows that fingering is enhanced for high concentrations at low temperatures, a point which will be returned to later. (Vancea et al.[25] explore in detail the effects of a range of simulation parameters on the tendency to form nanoparticle fingering patterns).

Figure 2 shows a morphology diagram resulting from varying chemical potential and temperature. There are two convenient boundaries in the chemical potential: one at the binodal line $\mu = 2\epsilon_l$ (as previously discussed) and the other at $\mu = 4\epsilon_l$. The latter boundary defines the chemical potential which exactly counteracts the liquid−liquid interactions of liquid cells with all nearest and next-nearest neighbors occupied by liquid cells. Hence, for $\mu \geq 4\epsilon_l$ the Metropolis acceptance probability of converting liquid to vapor is $p_{acc} = 1$. Liquid cells are instantly converted to vapor, nanoparticles are frozen at their initial random positions, and the system does not dewet by a suitable mechanism. This argument holds true for all liquid cells except those that wet nanoparticles. Hence, only extremely slow structural evolution via thermal coarsening is possible.

From Figure 2 it is possible to qualitatively visualize the transition from nucleation and growth dominated to spinodal dominated dewetting, with the spinodal line, $\mu_{sp}(T)$, separating these two regimes. It is evident that the spinodal line is temperature-dependent, and one could imagine extrapolating the shape of this transition curve to meet the temperature axis at $\mu_{sp}(0) = 4\epsilon_l$ and the binodal line close to a critical temperature $\mu_{sp}(T_c) = 2\epsilon_l$. For a simple lattice gas model $k_B T_c/\epsilon_l = 0.567$, which seems to be a good approximation to what is seen here. The region between the binodal and spinodal lines defines where the system is metastable, and the observed dewetting mechanism is nucleation and growth dominated. The transition from nucleation and growth to spinodal-dominated dewetting is not precise; a sharp definition between a metastable and a linearly unstable state is not observed, a result seen previously for deterministic continuum models of dewetting.[28] For low temperatures and chemical potential values close to the binodal line, the metastable nature of the system is evident; it remains a nanoparticle−solvent film without any dewetting occurring within 1000 MCS. Despite being at chemical potential values which are greater than the binodal value, the liquid state remains dominant as fluctuations in the system large enough to seed nucleation and growth are too infrequent to be observed on the time scale of our numerical experiments. For high temperatures, and chemical potential values well away from the binodal value, the system rapidly dewets via spinodal dewetting to leave small scale isolated wormlike domains and island structures.

In Figure 2, inset (a) highlights the chemical potential dependence, with three morphologies enlarged from the main figure. The three images are results of simulations with temperature $k_B T/\epsilon_l = 0.375$ and chemical potentials $\mu/\epsilon_l = 2.20$, 2.40, and 2.60, respectively. The transition from a cellular network to a labyrinthine structure (i.e., from nucleation and growth-dominated to spinodally dominated dewetting) is clear from the first two images. The third image highlights that further increasing μ produces wormlike domains, and eventually islands, with increasingly small characteristic length scales.

To further highlight the shape of the temperature-dependent spinodal line, and the behavior beyond this, inset (b) of Figure 2 shows a contour map of the Euler characteristic,[29,30] χ, normalized by the total number of nanoparticles, *N*, for the images shown in Figure 2. The Euler characteristic, sometimes referred to as the connectivity number, represents the connectivity of a binary image. In our case it signifies the number of bare substrate regions minus the number of enclosed nanoparticle regions. If liquid and nanoparticle are represented by white pixels and substrate by black pixels, then χ simply becomes the number of regions of connected black pixels minus the number of completely enclosed regions of white pixels. Prior to calculation of χ, 4-connected single pixel noise, mostly due to infrequent condensation of solvent at random sites, is removed from images. A small, positive value of χ indicates an interconnected nanoparticle structure such as that typically formed via nucleation and growth, and a large negative value of χ indicates a structure of many isolated nanoparticle domains/islands such as that typically formed via spinodal dewetting.

This is what is seen, as the positive values of χ are obtained for cellular network structures. However, noise still present in the images gives an overall reduction in χ, making absolute values less accurate, but relative comparison is still reliable. By normalizing χ with respect to the number of nanoparticles in the image, *N*, it is possible to extract important information from the values. $\chi/N \simeq 0$ gives an indication of a transition from nucleation and growth dominated to spinodal dominated dewetting, and $\chi/N \simeq -1$ implies a final morphology where all nanoparticles are completely separated from each other. $\chi/N = -0.44$ is the lowest value seen in Figure 2b due to the random initial positions of nanoparticles. The transition to spinodal-dominated dewetting causes a rapid decrease in χ/N as the connectivity of the nanoparticle structure is significantly reduced; this corresponds to the leftmost contour line. The shape of the contour lines beyond the spinodal line shows that further increasing μ results in a nearly linear decrease in the connectivity of the nanoparticle structure, something which is not immediately apparent from a rudimentary study of the morphologies. This close-to-linear relationship is perhaps surprising since the dependence of evaporation rate on chemical potential is

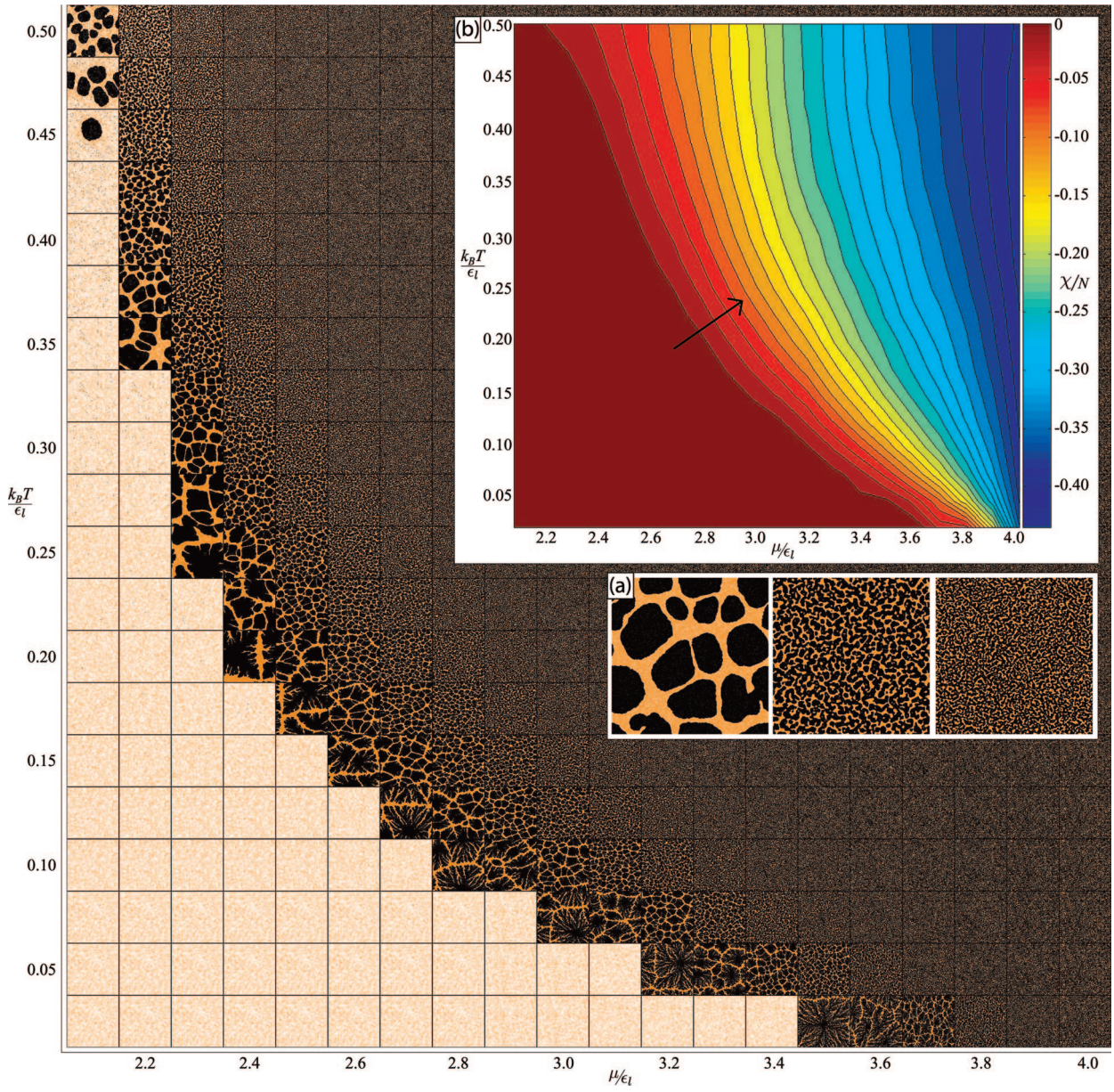

Figure 2. Morphology diagram resulting from varying chemical potential and temperature. All simulations were run on a 1024 × 1024 lattice with 25% nanoparticle concentration and $MR = 30$. Morphologies shown are representative of systems after bulk evaporation, but before significant thermal coarsening has occurred. This corresponds to less than 1000 MCS for most systems, except those that are nucleation and growth dominated which require up to 4000 MCS. Systems that showed no sign of dewetting after 1000 MCS (low chemical potential, low temperature) are displayed as wet nanoparticle−solvent films. Inset (a) displays three morphologies obtained at $k_BT/\epsilon_l = 0.375$ with chemical potentials $\mu/\epsilon_l = 2.20$, 2.40, and 2.60, respectively. Inset (b) shows a contour plot of normalized Euler characteristic, χ/N. The arrow indicates the direction of decreasing χ/N with contour lines every 0.02 units. The abrupt change in χ/N indicates the spinodal line; at low μ, χ/N varies little between the binodal and spinodal line, but increasing μ beyond the spinodal line results in a nearly linear decrease in χ/N. The sharp increase in χ/N is not due to the transition from wet to dry systems (see Figure 1 of Supporting Information).

highly nonlinear. It is clear that further systematic analysis of the dependence of the Euler characteristic (and the other 2D Minkowski measures[29,30]) on not only the chemical potential but also variables such as the nanoparticle coverage is required (and is planned). On this point, we note that Mecke and Sofonea[30] have carried out a detailed systematic analysis, using Minkowski measures, of the morphology of systems which phase separate by spinodal decomposition. They have determined the relationship between the Euler characteristic and the mean density, observing that χ is zero for symmetric decomposition and varies approximately linearly as the mean density is varied across a wide range.

B. Coexisting Patterns. The influence of modeling a thickness-dependent disjoining pressure will now be explored. Here, we couple the chemical potential to the solvent density using a sigmoidal (step) function of the form

$$\mu(\nu) = \mu_0\left(1 + \frac{\Delta\mu_f}{1 + e^{-(\nu-\nu_s)/\sigma}}\right) \quad (3)$$

where ν is the vapor fraction of the solvent, μ_0 is the initial value of the chemical potential, and $\Delta\mu_f$ is a fractional increase in chemical potential which occurs around the vapor fraction ν_s with a sharpness of σ—essentially step height, position, and width. We choose this sigmoidal function to model two distinct regimes of dewetting, informed by an inspection of the

experimental AFM data. For dual-scale patterning we require two distinct rates of evaporation in the simulation, similar to the decoupling of hole growth and bulk evaporation in the model of Yosef and Rabani.[19] In the 2D model of Rabani et al.,[17] μ represents an effective chemical potential comprising (i) the "true" liquid−gas chemical potential and (ii) homogeneous interaction of liquid with the substrate. A comparison of experiments and continuum thin film models indicates that the film−substrate interaction below 10 nm thickness may change dramatically with thickness as different long-range/short-range interactions dominate at different thicknesses.[31] Continuum models absorb these effects into a so-called thickness-dependent disjoining pressure. Taking the mean liquid concentration as a measure of ultrathin film thickness, one wants to account for the dominance of different substrate−film interactions. The simplest way to do this is by switching contribution (ii) of the effective chemical potential between two values. As the simulation proceeds, the solvent density decreases as liquid cells are converted to vapor and ν increases. As ν approaches ν_s, the chemical potential increases in magnitude such that conversion of solvent from the liquid to vapor phase occurs more frequently. This shift in evaporation rate alters the dewetting mechanism and, hence, controls the final morphology of the deposited nanoparticles. By using the dynamical form of the chemical potential shown in eq 3, it is possible to move through the parameter space associated with Figure 2 during the course of a single simulation to reproduce patterns with two characteristic length scales. It is even possible to traverse the spinodal line during a simulation to create morphologies where both nucleation and growth and spinodal dewetting patterns coexist, as observed in experimental dewetting systems such as the aqueous collagen solutions studied by Thiele et al.[31] and metal films studied by Herminghaus et al.[32] where different disjoining pressure contributions are responsible for the two-level patterning that is produced via the two dewetting mechanisms.

1. Dual-Scale Cellular Networks. The first type of dual-scale pattern we shall discuss is the cellular network. This structure is commonly observed when, for example, spin-coating thiol-passivated gold nanoparticles onto silicon substrates from solvents such as toluene or hexane. The structure is similar to a standard cellular network with the exception that the distribution of cell sizes is bimodal, i.e., has two maxima. Figure 3a shows the result of a simulation using a dynamic chemical potential. It is accompanied by Figure 3b, a tapping-mode atomic force microscope (TM-AFM) image of chloroform-dispersed octanethiol-passivated 2 nm gold nanoparticles spin-coated onto silicon oxide. The correspondence between the two images is strong; the larger cell size component of the image is dominant, and the smaller cell size features are grouped together in randomly positioned patches. The sigmoidal form of the dynamic chemical potential allows for the formation of a pattern with a bimodal distribution of cell sizes as follows. The simulation commences, and slow thermal nucleation occurs at random positions across the film. Holes in the thin film then grow to form a cellular network structure. However, as the vapor fraction of the solvent, ν, approaches ν_s, the chemical potential μ increases in magnitude. This moves the system toward the linearly unstable spinodal regime, and thus holes open up in the solvated regions of the film within a narrow time window. This produces small scale holes formed in patches of the nanoparticle−solvent film that underwent dewetting at late times. Thus, a pattern is created with two distinct regions: one characteristic of the initial chemical potential and one characteristic of the final chemical potential, with the relative fraction of each pattern controlled by ν_s and the degree by which the two patterns merge together controlled by σ.

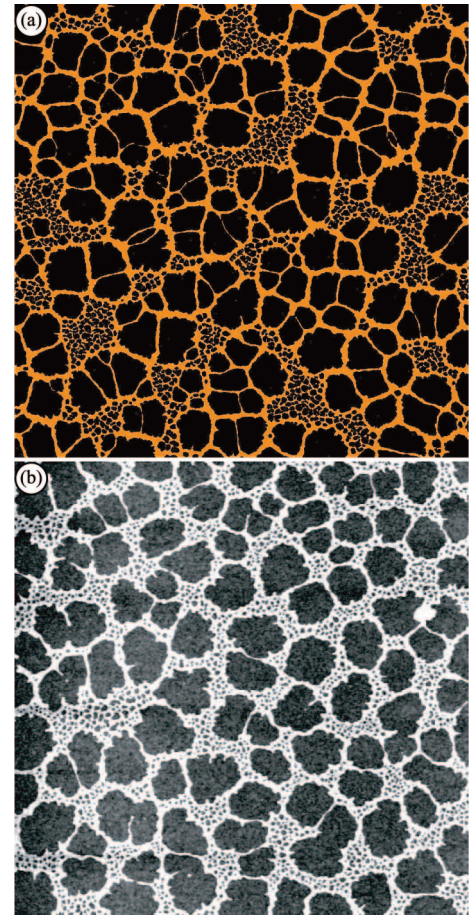

Figure 3. Dual-scale cellular networks. (a) The result of a simulation on a 4096 × 4096 lattice using $k_BT/\epsilon_1 = 0.29$, $\mu_0/\epsilon_1 = 2.30$, 25% nanoparticle concentration, and $MR = 25$, with a dynamic chemical potential using parameters $\Delta\mu_f = 0.10$, $\nu_s = 0.70$, and $\sigma = 0.01$. Video 1 of the Supporting Information shows the formation of such a structure. (b) 5 μm^2 TM-AFM image of 2 nm core-size octanethiol-passivated gold nanoparticles spin-coated from chloroform (concentration 1 mg/mL) onto silicon with a thick, 300 nm thermal oxide layer. A sharp transition of the system from nucleation and growth-dominated toward spinodal-dominated dewetting can explain the bimodal distribution of cell sizes.

Figure 4a shows a morphology diagram associated with two of the variables in the functional form of the chemical potential, ν_s and $\Delta\mu_f$. At the initial value of the chemical potential, μ_0, dewetting is nucleation and growth-dominated. As the vapor fraction approaches ν_s, the dewetting behavior changes, the extent of which is dependent on $\Delta\mu_f$. When $\Delta\mu_f = 0.05$, the increase in chemical potential magnitude is small, and so dewetting is still nucleation and growth-dominated. However, when $\Delta\mu_f = 0.25$, the chemical potential switch is great enough such that the dewetting regime becomes spinodal-dominated. It is clear from Figure 4a that ν_s simply controls the relative proportions of the two type of patterning. Figure 4b shows an example of the functional form of the chemical potential. In this case, a sharp, steplike function used to obtain the central morphology of Figure 4a is shown.

2. Nanoparticle Rings. It can be seen from Figure 4a that with $\nu_s = 0.10$ and $\Delta\mu_f = 0.25$ nanoparticle rings are formed, isolated from each other by a wormlike spinodal dewetting pattern. The formation of large, micrometer-sized nanoparticle rings has been observed previously for a number of drying

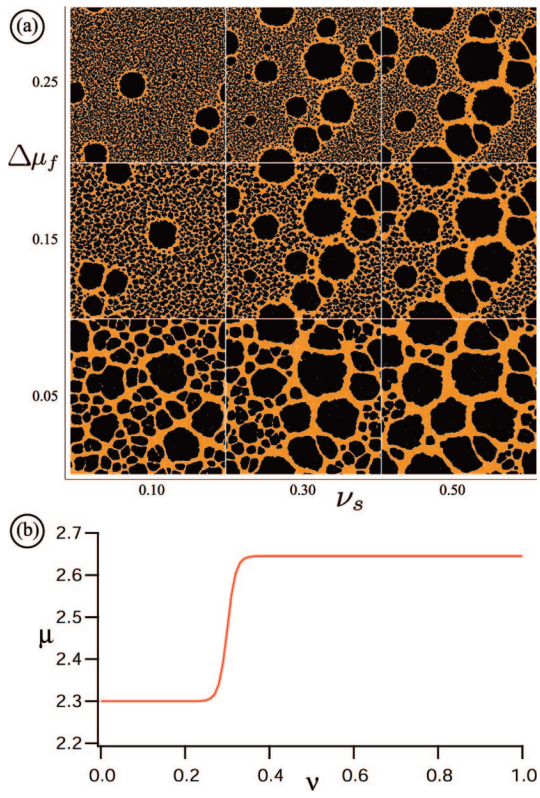

Figure 4. (a) Morphology diagram associated with varying two parameters which control the dynamic chemical potential. All simulations were run on a 1024 × 1024 lattice with 30% nanoparticle concentration, $MR = 30$, $k_BT/\epsilon_1 = 0.3$, $\mu_0/\epsilon_1 = 2.30$, $\sigma = 0.01$, and until complete solvent evaporation. (b) An example of the chemical potential functional form with parameters $\Delta\mu_f = 0.15$, $\nu_s = 0.30$, and $\sigma = 0.01$.

nanoparticle−solvent systems.[1,2,4,5] Successful numerical modeling of nanoparticle ring structures was first achieved by Yosef and Rabani[19] in their fully 3D simulation model, which involves two separate evaporation rates: one controlling hole growth and the other controlling the global thinning of the solvent film. While our model also captures thermally activated hole nucleation, the same process in the 3D model is significantly slower. The precise mechanism of hole formation in the experiments is not entirely clear—defect-mediated and thermally driven nucleation are both possible.

In our experiments, spin-coating nanoparticles dissolved in highly volatile solvents such as dichloromethane and chloroform tends to give rise to nanoparticle rings. The formation of these rings can be described by a nucleation and growth mechanism. A hole is nucleated in the thin nanoparticle−solvent film (via evaporation or the presence of a defect), and then solvent evaporates isotropically to create a circular front carrying nanoparticles outward. In previous simulations by Yosef and Rabani,[19] the growth of these rings is arrested via global removal of solvent, as is the case in our model by construction. When solvent evaporation is complete, nanoparticles are deposited in the form of a ring. The nucleation and growth of nanoparticle rings occurs if the thin film is initially metastable. In our model, infrequent thermal nucleation of the metastable solvent film causes a few randomly positioned holes to form. As the simulation progresses, these nanoparticle rings grow, but due to the steplike dependence of the chemical potential on ν, at a critical solvent coverage the system is driven from nucleation and growth-dominated to spinodal-dominated dewetting. In the case of a large enough $\Delta\mu_f$, the remaining nanoparticle−solvent film becomes unstable and dewets via a spinodal mechanism; this is the case for Figure 5a.

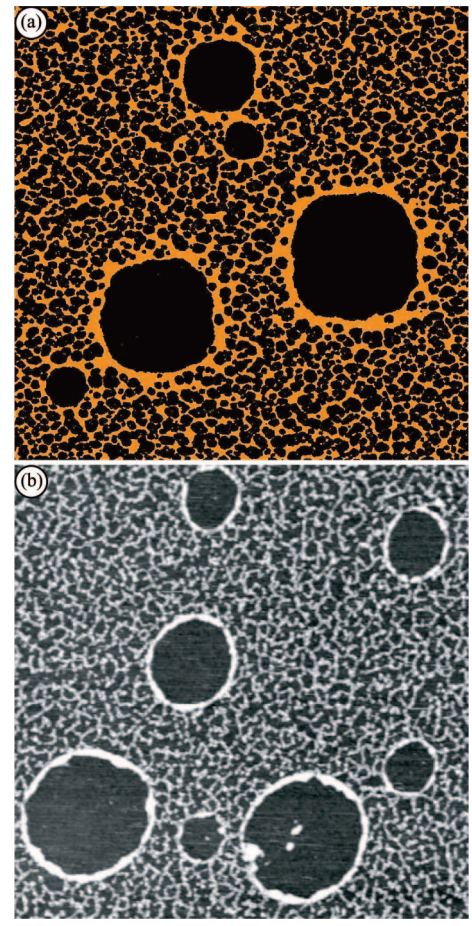

Figure 5. Nanoparticle rings. (a) The result of a simulation on a 2048 × 2048 lattice using $k_BT/\epsilon_1 = 0.26$, $\mu_0/\epsilon_1 = 2.30$, 25% nanoparticle concentration, and $MR = 100$, with a dynamic chemical potential using parameters $\Delta\mu_f = 0.15$, $\nu_s = 0.15$, and $\sigma = 0.01$. Video 2 of the Supporting Information shows the formation of this structure. (b) 3.5 μm^2 TM-AFM image of 2nm core-size octanethiol-passivated gold nanoparticles spin-coated from chloroform (concentration 1 mg/mL) onto silicon with a thin, 2 nm native oxide layer. Most nanoparticle rings appear to have been thermally nucleated as there is no evidence of surface defects at their centers. A transition of the system from a metastable to a linearly unstable state can explain the coexistence of nanoparticle rings and small scale patterning.

Figure 5b shows a TM-AFM image of nanoparticle rings coexisting with small scale patterning resulting from 2 nm core-size octanethiol-passivated gold nanoparticles spin-coated from chloroform onto silicon with a thin, 2 nm native oxide layer. The agreement between simulation and experimental images is strong. The coexistence of patterning due to two different dewetting mechanisms is clear, and the reason for choosing a sigmoidal form for the chemical potential is particularly apparent from Figure 5b. There are clearly two distinct types of patterning which a sharp, step function is capable of reproducing at the initial and final values, reflecting a sharp increase in the disjoining pressure as the film thins.

A mechanism for ring formation in nanoparticle−solvent films was proposed by Ohara and Gelbart.[2] They conclude that as rings grow, the increasing density of nanoparticles at the rim increases the frictional force between nanoparticles and the surface, which arrests the growth of the rings. This would lead to an upper limit on the size of nanoparticle rings with a given density of nanoparticles in solution. From a 3D Monte Carlo

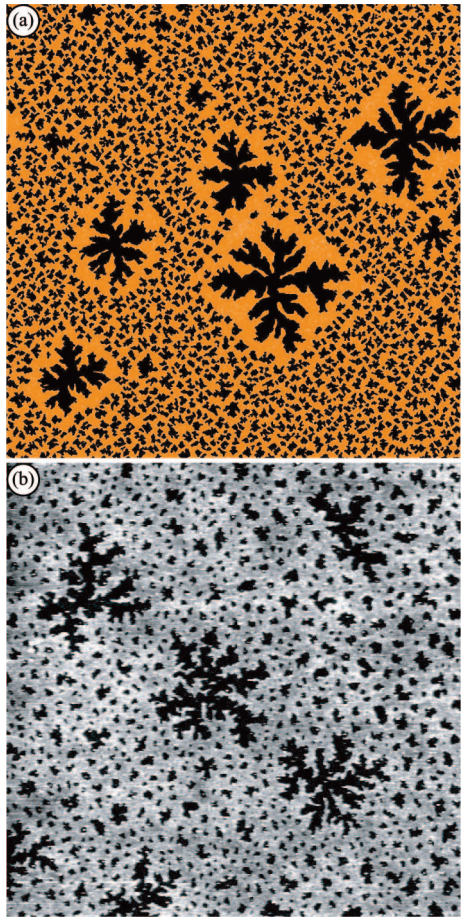

Figure 6. Nanoparticle fingering. (a) The result of a simulation on a 2048 × 2048 lattice using $k_BT/\epsilon_1 = 0.235$, $\mu_0/\epsilon_1 = 2.40$, 55% nanoparticle concentration, $MR = 2$, and with a dynamic chemical potential using parameters $\Delta\mu_f = 0.15$, $\nu_s = 0.20$, and $\sigma = 0.02$. Video 3 of the Supporting Information shows the formation of this structure. (b) 5.5 μm^2 TM-AFM image of 2 nm core-size dodecanethiol-passivated gold nanoparticles deposited from toluene (concentration 0.5 mg/mL) onto silicon with a thin, 2 nm native oxide layer via meniscus-driven evaporation—a technique described by Pauliac-Vaujour and Moriarty.[13] A transition from nucleation and growth to spinodal dominated dewetting in a system with high nanoparticle concentration can explain the coexisting patterns observed here.

simulation, Yosef and Rabani[19] find that the increasing density of nanoparticles at the rim plays an insignificant role in arresting ring growth. They claim that global evaporation of the thin liquid film stops the ring growth. For the sample shown in Figure 5b, nanoparticle ring diameters have an upper limit of ~1 μm. In our case, we cannot yet ascertain which of these mechanisms plays the dominant role. Heterogeneous nucleation combined with either a small window of metastability or an upper limit of ring diameter will lead to the same result; either (or both) of these may be at work here. Our simulation model cannot in principle give the answer as growth is arrested via global evaporation by construction. Although the inclusion of a parameter in the model which specifically takes account of the nanoparticle−substrate interaction may be helpful in distinguishing between the two mechanisms, recent experiments in our laboratory indicate that solvent hydrodynamics influence ring formation. Thus, only by including aspects of a continuum model, such as convective liquid motion, is it likely that a definitive distinction between the two mechanisms can be made.

Attempts to simulate nanoparticle ring structures have been unsuccessful in fully capturing their circular nature—a consequence of a model on a square lattice. Including next-nearest neighbor interactions is necessary to better imitate isotropic growth of holes in a thin film, and therefore a suitable weighting of interactions must be found. This study, and previous work,[14,19,26] have weighted the interaction energies linearly with distance (a $1/\sqrt{2}$ factor for next-nearest-neighbor interactions) which greatly improves the situation, but to achieve maximum possible isotropy for a model with nearest- and next-nearest-neighbor interactions only, the growth rate of holes must be equal in the four grid directions and the diagonals.

3. Nanoparticle Fingers. As mentioned earlier, the mobility ratio (*MR*) gives control over the relative rates of nanoparticle diffusion and solvent evaporation. With a high enough *MR*, nanoparticles are able to diffuse away from retreating liquid fronts remaining well-solvated, resulting in nanoparticle rings. However, as this ratio is lowered, nanoparticles become less mobile and cannot diffuse away fast enough from retreating liquid fronts. The liquid−vapor interface becomes unstable and develops undulations, and nanoparticles are deposited in the form of fingers, i.e., nanoparticle aggregations forming perpendicular to the direction of the retreating interface.[8,25] In 2006, Yosef and Rabani[19] described this formation process with respect to their 3D lattice gas-based model. The mobility ratio allows us direct control over the tendency to form fingering structures. However, it is not the only parameter of interest; increasing the nanoparticle concentration also results in the emergence of fingering patterns, as is clear from Figure 1. This is due to nanoparticle mobility being reduced via the presence of other nanoparticles; they simply have nowhere to move to. Indeed, it is seen in experiments that fingering is observed when the areal coverage of nanoparticles is high.[8]

Figure 6a shows the result of a simulation where a number of nanoparticle fingering patterns are present among a high areal density of small scale voids. Figure 6b is the corresponding experimental image. The sample shown in Figure 6b was prepared via meniscus-driven evaporation within a Teflon ring[13] of 2 nm core-size dodecanethiol-passivated gold nanoparticles dispersed in toluene. This deposition method allows different patterns to be observed at various distances from the ring's center. Fingering patterns are observed near the edge of the ring where evaporation is relatively slow and nanoparticle concentration is high. Correspondingly, the simulation is run at low temperature with high nanoparticle concentration. The use of decanethiol for nanoparticle passivation promotes greater ligand interdigitation which results in lower nanoparticle mobility.[8] In Figure 6a, buildup of nanoparticles around the fingering structures is an unavoidable consequence of the conditions required to generate these morphologies within this model.

The description of the formation of this pattern is essentially the same as that for nanoparticle rings, except that when the mobility ratio is reduced the interface of the expanding hole becomes unstable and develops fingers. Nucleation and growth is responsible for nanoparticle fingering, and then a switch in chemical potential through the spinodal point gives rise to the secondary structure, which, as shown earlier, gives rise to voids if the concentration of nanoparticles is high enough.

IV. Conclusions

Dual-scale pattern formation in drying colloidal nanoparticle solutions has been studied via a pseudo-3D lattice gas-based simulation. The results of the simulations correlate well with many experimentally studied dewetting systems.[1,2,4,5,8,14,31,32] The formation of dual-scale cellular networks and nanoparticle rings and fingering structures coexisting with small scale patterning

has been achieved via coupling the chemical potential to the solvent density. The clear disparity in the two types of experimental coexisting patterns indicates a sharp transition in dewetting mechanism. The use of a sigmoidal chemical potential form allows for an initial state of the film to be metastable and the final state to be linearly unstable if the spinodal point is passed. This leads to the coexistence of patterns formed via nucleation and growth and spinodal dominated dewetting mechanisms.

Anisotropy is still evident in this model; it is particularly apparent in ring growth. As mentioned previously, to achieve maximum possible isotropy for consideration of nearest and next-nearest neighbors only, liquid−vapor interfaces which are horizontal or vertical must advance/recede at the same rate as any diagonal interface. Since a step in a diagonal direction is $\sqrt{2}$ times greater than in a horizontal or vertical direction, and interface growth rates are proportional to Boltzmann factors, the weighting of next-nearest interactions should be chosen such that Boltzmann factors associated with diagonal moves are $\sqrt{2}$ times less than those for horizontal or vertical moves. A second criterion for isotropy is that the interfacial energy per unit length is equal for horizontal/vertical and diagonal liquid−vapor interfaces. A further consideration is the anisotropy of nanoparticle diffusion; the need to include diagonal diffusive steps of nanoparticles becomes more apparent at high nanoparticle densities.

The results of these simulations give important insights into dewetting processes for real experiments where a thickness-dependent disjoining pressure can result in a sharp transition from a nucleation and growth-dominated to a spinodal-dominated regime in a thinning nanoparticle−solvent film.

Acknowledgment. We are grateful for the financial support of the UK Engineering and Physical Sciences Research Council and the EU Framework Programme 6: Marie Curie Research Training Networks scheme (under Grant MRTN-CT-2004-005728 (PATTERNS)). EPSRC is also thanked for the provision of studentships for A.S. and C.P.M.

Supporting Information Available: Videos showing the formation of the simulated structures shown in Figures 3a, 5a, and 6a as well as additional information related to Figure 2. This material is available free of charge via the Internet at http://pubs.acs.org.

References and Notes

(1) Ohara, P. C.; Heath, J. R.; Gelbart, W. M. *Angew. Chem., Int. Ed.* **1997**, *36*, 1078.
(2) Ohara, P. C.; Gelbart, W. M. *Langmuir* **1998**, *14*, 3418.
(3) Ge, G.; Brus, L. *J. Phys. Chem. B* **2000**, *104*, 9573.
(4) Maillard, M.; Motte, L.; Ngo, A. T.; Pileni, M. P. *J. Phys. Chem. B* **2000**, *104*, 11871.
(5) Maillard, M.; Motte, L.; Pileni, M. P. *Adv. Mater.* **2001**, *13*, 200.
(6) Stowell, C.; Korgel, B. *Nano Lett.* **2001**, *1*, 595.
(7) Moriarty, P.; Taylor, M. D. R.; Brust, M. *Phys. Rev. Lett.* **2002**, *89*, 248303.
(8) Pauliac-Vaujour, E.; Stannard, A.; Martin, C. P.; Blunt, M. O.; Notinger, I.; Moriarty, P. J.; Vancea, I.; Thiele, U. *Phys. Rev. Lett.* **2008**, *100*, 176102.
(9) Lin, X.-M.; Jaeger, H. M.; Sorensen, C. M.; Klabunde, K. J. *J. Phys. Chem. B* **2001**, *105*, 3353.
(10) Bigioni, T.; Lin, X.-M.; Nguyen, T. T.; Corwin, E. I.; Witten, T. A.; Jaeger, H. M. *Nat. Mater.* **2006**, *5*, 265.
(11) Huang, J.; Kim, F.; Tao, A. R.; Connor, S.; Yang, P. *Nat. Mater.* **2005**, *4*, 896.
(12) Xu, J.; Xia, J.; Hong, S. W.; Lin, Z.; Qiu, F.; Yang, Y. *Phys. Rev. Lett.* **2006**, *96*, 066104.
(13) Pauliac-Vaujour, E.; Moriarty, P. J. *J. Phys. Chem. C* **2007**, *111*, 16255.
(14) Martin, C. P.; Blunt, M. O.; Pauliac-Vaujour, E.; Stannard, A.; Moriarty, P.; Vancea, I.; Thiele, U. *Phys. Rev. Lett.* **2007**, *99*, 116103.
(15) Lu, N.; Xiaodong, C.; Molenda, D.; Naber, A.; Fuchs, H.; Talapin, D. V.; Weller, H.; Muller, J.; Lupton, J. M.; Feldmann, J.; Rogach, A. L.; Chi, L. *Nano Lett.* **2004**, *4*, 885.
(16) Blunt, M. O.; Martin, C. P.; Ahola-Tuomi, M.; Pauliac-Vaujour, E.; Sharp, P.; Nativo, P.; Brust, M.; Moriarty, P. J. *Nat. Nanotechnol.* **2007**, *2*, 167.
(17) Rabani, E.; Reichman, D. R.; Geissier, P. L.; Brus, L. E. *Nature (London)* **2003**, *426*, 271.
(18) Sztrum, C. G.; Hod, O.; Rabani, E. *J. Phys. Chem. B* **2005**, *109*, 6741.
(19) Yosef, G.; Rabani, E. *J. Phys. Chem. B* **2006**, *110*, 20965.
(20) Kletenik-Edelman, O.; Ploshnik, E.; Salant, A.; Shenhar, R.; Banin, U.; Rabani, E. *J. Phys. Chem. C* **2008**, *112*, 4498.
(21) Ge, G.; Brus, L. E. *Nano Lett.* **2001**, *1*, 219.
(22) Israelachvili, J. *Intermolecular and Surface Forces*, 2nd ed.; Academic: London, 1992.
(23) de Gennes, P. G. *Rev. Mod. Phys.* **1985**, *57*, 827.
(24) Thiele, U. *Eur. Phys. J. E* **2003**, *12*, 409.
(25) Vancea, I.; Thiele, U.; Pauliac-Vaujour, E.; Stannard, A.; Martin, C. P.; Blunt, M. O.; Moriarty, P. J. *Phys. Rev. E*, in press (2008).
(26) Martin, C. P.; Blunt, M. O.; Moriarty, P. *Nano Lett.* **2004**, *4*, 2389.
(27) Siepmann, P.; Martin, C. P.; Vancea, I.; Moriarty, P. J.; Krasnogor, N. *Nano Lett.* **2007**, *7*, 1985.
(28) Thiele, U.; Velarde, M. G.; Neuffer, K. *Phys. Rev. Lett.* **2001**, *87*, 016104.
(29) Michielsen, K.; De Raedt, H. *Phys. Rep.* **2001**, *347*, 461.
(30) Mecke, K. R.; Sofonea, V. *Phys. Rev. E* **1997**, *56*, R3761.
(31) Thiele, U.; Mertig, M.; Pompe, W. *Phys. Rev. Lett.* **1998**, *80*, 2869.
(32) Herminghaus, S.; Jacobs, K.; Mecke, K.; Bischof, J.; Fery, A.; Ibn-Elhaj, M.; Schlagowski, S. *Science* **1998**, *282*, 916.

JP803399D